



# Metal nanoparticles decorated MIL-125-NH<sub>2</sub> and MIL-125 for efficient photocatalysis

Jianhao Qiu, Lvye Yang, Ming Li, Jianfeng Yao\*

College of Chemical Engineering, Jiangsu Key Lab for the Chemistry & Utilization of Agricultural and Forest Biomass, Jiangsu Key Lab of Biomass-based Green Fuels and Chemicals, Nanjing Forestry University, Nanjing, Jiangsu, 210037, China



## ARTICLE INFO

### Keywords:

MIL-125-NH<sub>2</sub>  
MIL-125  
Metal loading  
Photocatalysis

## ABSTRACT

Metal nanoparticles (NPs) decorated MOFs for photocatalysis has drawn enormous attention in the past decade. Here, a series of M/Ti-MOFs (M = Pt and Au, Ti-MOFs = MIL-125-NH<sub>2</sub> and MIL-125) has been synthesized through a facile post-synthetic method and the metal NPs highly dispersed on surface of MOFs with major sizes of 3–9 nm. Light absorption edges of scaffolds are crucial in the photocatalytic oxidation of benzyl alcohol over M/MIL-125-NH<sub>2</sub> and M/MIL-125. The conversion of benzyl alcohol over Pt/MIL-125-NH<sub>2</sub> is 2.4 times and 1.9 times higher than that of pristine MIL-125-NH<sub>2</sub> and Au/MIL-125-NH<sub>2</sub>, respectively. Besides, Pt/MIL-125-NH<sub>2</sub> photocatalyst also exhibited good activity for Cr(VI) reduction compared to that of MIL-125-NH<sub>2</sub>. The enhanced photocatalytic activity of Pt/MIL-125-NH<sub>2</sub> is contributed to the rapid transfer of photo-induced electrons and decreased recombination of electron-hole pairs, which is verified by measurements of photocurrent and Electrochemical Impedance Spectroscopy. We hope that this study will provide worthy information for designing metal/MOFs or metal/MOFs-NH<sub>2</sub> photocatalysts.

## 1. Introduction

Metal-organic frameworks (MOFs), a new class of porous crystalline networks assembled by inorganic vertices and organic struts, have been extensively researched in the past decades. Owing to their outstanding properties including large surface areas, well-ordered porosity and tunable molecular structure, MOFs have been applied in numerous fields, such as separation and adsorption [1–3], drug delivery [4], chemical sensors [5] and heterogeneous catalysis [6–9]. As one of the typical heterogeneous catalysis, photocatalysis is famous for its pollution-free and economy compared to the conventional reaction [10,11]. The large surface area and flexible band gap of MOFs endow them great potential for photocatalysis [12–17]. Thus, there are several kinds of MOFs, e. g. MILs, UiOs and ZIFs, have been extensively utilized in this field [9]. Among them, Ti-MOFs (MIL-125 and MIL-125-NH<sub>2</sub>) for photocatalysis are gradually becoming popular owing to the glorious optical properties of titanium center [18]. In 2012, MIL-125-NH<sub>2</sub> was firstly synthesized for photocatalytic reduction of CO<sub>2</sub> [19] and then utilized for photocatalytic oxidation of amines to imines [20]. For instance, Wang and co-workers utilized different semiconductors including metal sulphides (MoS<sub>2</sub>, Ag<sub>2</sub>S, CdS and CuS) [21], g-C<sub>3</sub>N<sub>4</sub> [22] and In<sub>2</sub>S<sub>3</sub> [23] to combine with MIL-125 for Cr(VI) reduction, dyes and tetracycline removal. Pristine MOFs undergo little visible-light

absorption and rapid electron-hole pairs recombination. Therefore, MOFs decoration is an significant route to settle above problems [9].

Lots of modified strategies have emerged with the rapid development of photocatalysts based on MOFs, e. g. decoration of metal centers or linkers, combination with semiconductors, metal nanoparticles (NPs) loading, sensitization and pyrolyzation. Thereinto, metal NPs loading is regarded as one of the most efficient approaches owing to their large surface area, more exposure of reaction sites and the high density of the coordination unsaturated sites. However, metal NPs are tended to migration and aggregation due to their high surface energy [24]. Metal NPs loading on MOFs could divide into the following ways: dispersion on the surface [25,26] and encapsulation into the cavities [27–31]. To the surface loading, large surface areas and narrow micropore distribution of MOFs may restrain the migration and aggregation of metal NPs compared to the conventional scaffolds (e. g. TiO<sub>2</sub>, ZnO and CdS), resulting in well dispersed NPs. Li et al. developed double-solvent impregnation method for metal encapsulation into cavities (Pd@MIL-100, PdAu@MIL-100 and CuPd@UiO-66-NH<sub>2</sub>) on N-alkylation of amines with alcohols (Conversion: > 99%) and Suzuki Coupling Reaction (Conversion: 99%) [29,28–31]. Encapsulating metal NPs into the cavities of MOFs will prevent the loss of NPs efficiently and verify the excellent recycling test, but the specific window size (3.4 Å for ZIF-8 and 6 Å for UiO-66) limits its general applicability. Therefore, many

\* Corresponding author.

E-mail address: [jfyao@njfu.edu.cn](mailto:jfyao@njfu.edu.cn) (J. Yao).

reports were focused on the metal NPs surface loading. Horiuchi and co-workers deposited Pt NPs as co-catalysts onto MIL-125-NH<sub>2</sub> by a photodeposition process for visible-light-promoted photocatalytic hydrogen production [32]. Ag/MIL-125-NH<sub>2</sub> has been synthesized in situ by the reduction of Ag<sup>+</sup> with the acetylacetonate pendant groups and the nanocomposites showed efficient methylene blue photocatalytic degradation [33]. Shen et al. synthesized M/MIL-125 (M = Au, Pd, Pt) composites via redox reaction between the reductive MIL-125 with Ti<sup>3+</sup> and oxidative metal salt precursors for benzyl alcohol photocatalytic oxidation [34]. However, the comprehensive studies and comparison focused on different noble metal particles (Pt or Au) loading on MIL-125 with and without amino-functionalization for the benzyl alcohol oxidation have not been studied. In addition, MIL-125-NH<sub>2</sub> decorated by metal nanoparticles for Cr(VI) photocatalytic reduction has not been investigated either.

Here, a series of M/Ti-MOFs (M = Pt and Au, Ti-MOFs = MIL-125-NH<sub>2</sub> and MIL-125) photocatalysts has been synthesized by a facile post-synthetic method for the selective oxidation of benzyl alcohol. Results demonstrate that (1) the photocatalytic activity of metal loading on MIL-125-NH<sub>2</sub> is higher than that of MIL-125, (2) Pt/MIL-125-NH<sub>2</sub> performs much higher photocatalytic activity than that of Au/MIL-125-NH<sub>2</sub> and MIL-125-NH<sub>2</sub> for benzyl alcohol oxidation. In addition, Pt/MIL-125-NH<sub>2</sub> also performed high activity for Cr(VI) photocatalytic reduction. In order to verify the decreased recombination of photo-induced electrons and holes, photocurrent and Electrochemical Impedance Spectroscopy measurements have been carried out and a possible mechanism for the improved photocatalytic activity has been given.

## 2. Experimental

### 2.1. Materials

Titanium isopropoxide (Ti(O-*i*Pr)<sub>4</sub>, 99%) was obtained from Sam Chemical Technology (Shanghai) Co., Ltd. Poly (diallyldimethylammonium chloride) solution (Mw 200000-350000, 20 wt%, (C<sub>8</sub>H<sub>16</sub>ClN)<sub>n</sub>, PDDA) and Chloroplatinic acid hexahydrate (H<sub>2</sub>PtCl<sub>6</sub>·6H<sub>2</sub>O, Pt ≥ 37.5%) were purchased from Aladdin Industrial Company, China. 1,4-benzendicarboxylic acid, N, N-dimethylformamide (DMF), Sodium borohydride (NaBH<sub>4</sub>, 98%), NaOH and methanol were supplied by Sinopharm Chemical Reagent Co., Ltd., China. Hydrogen Tetrachloroaurate (III) Trihydrate (HAuCl<sub>4</sub>·3H<sub>2</sub>O) was obtained from Shanghai Titan Scientific Co., Ltd., China. All chemicals were used as received without further treatment.

### 2.2. Synthesis of Ti-MOFs (MIL-125 and MIL-125-NH<sub>2</sub>)

MIL-125 and MIL-125-NH<sub>2</sub> were synthesized referring to previous report [35]. In a typical synthesis, 1.6 mL of Ti(O-*i*Pr)<sub>4</sub> and 3 g of 1,4-benzendicarboxylic acid were dissolved in 56 mL of DMF solution containing 6 mL of methanol, and then continuous stirring for 2 h. After that, the mixed solution was placed into a 100 mL Teflon-lined stainless steel autoclave and heated at 150 °C for 48 h. The solid products were collected by centrifugation and washed with DMF and methanol to remove the residual reactant and exchange the DMF. MIL-125-NH<sub>2</sub> was synthesized by the same method with 3.3 g of 2-NH<sub>2</sub>-terephthalic acid and 72 h instead of 3 g of 1,4-benzendicarboxylic acid and 48 h heating time, respectively.

### 2.3. Preparation of Pt and Au NPs solution

The Pt and Au NPs solutions in a homogeneous dispersion were prepared based on a previous report with modifications [36]. Typically, 2 mL of KOH solution (0.1 mol·L<sup>-1</sup>) added into 26 mL of H<sub>2</sub>PtCl<sub>6</sub>·6H<sub>2</sub>O with a concentration of 3.8 × 10<sup>-3</sup> mol·L<sup>-1</sup>. After vigorous stirring of 15 min, 10 mL of PDDA aqueous solution (0.02 g·mL<sup>-1</sup>) was added into

the above solution and stirred for another 15 min. Finally, 10 mL of NaBH<sub>4</sub> aqueous solution (0.35 mol·L<sup>-1</sup>) was added into the mixture drop by drop with a time interval of 3 s and a constant vigorous stirring. Au NPs solution was synthesized by the same method with HAuCl<sub>4</sub>·3H<sub>2</sub>O instead of H<sub>2</sub>PtCl<sub>6</sub>·6H<sub>2</sub>O.

### 2.4. Synthesis of M/Ti-MOFs (Pt/MIL-125-NH<sub>2</sub>, Au/MIL-125-NH<sub>2</sub>, Pt/MIL-125 and Au/MIL-125)

M/Ti-MOFs were prepared by a facile method. Typically, 250 mg of MIL-125 or MIL-125-NH<sub>2</sub> was added into 6.2 mL as-prepared Pt or Au solution (1 wt% to Ti-MOFs). Then the mixture was stirred for 1 h followed by 1 h ultrasonic treatment and the same processes were repeated for three times. The resulting mixture was washed by deionized water and ethanol for several times and then dried at 80 °C overnight. The obtained Pt/MIL-125-NH<sub>2</sub>, Au/MIL-125-NH<sub>2</sub>, Pt/MIL-125 and Au/MIL-125 samples (the estimated loading amounts of Pt or Au on MIL-125-NH<sub>2</sub> are 0.68% and 0.76% respectively, which were evaluated by XPS measurement) were marked as PtMN, AuMN, PtM and AuM, respectively.

### 2.5. Characterization

The crystalline structures of these samples were measured by X-ray diffraction (XRD) using Rigaku Ultima IV with Cu K $\alpha$  radiation ( $k = 0.1542$  nm) at 40 kV. The Energy Dispersive X-Ray (EDX) Fluorescence Spectrometer of the samples was observed by utilizing a JSM-7600 F (JEOL Ltd., Japan) with an operating voltage of 30 kV. Transmission electron microscopy (TEM) image and high-resolution transmission electron microscope (HRTEM) were examined by a JEOL JEM-2100 instrument at the accelerating voltage of 200 kV. Nitrogen adsorption-desorption analysis was conducted using Micromeritics ASAP 2020 at 77 K. All samples were degassed at 120 °C for 120 min prior to analysis. The specific surface areas were calculated by the Brunauer-Emmett-Teller (BET) method. X-ray photoelectron spectroscopy (XPS, AXIS UltraDLD, Japan) was employed to determine surface electronic states. All the binding energies were referenced to the C1 s peak at 284.8 eV of the surface adventitious carbon. The UV-vis diffuse reflectance spectra (DRS) of the samples over a range of 200–800 nm were recorded by UV-2600 (Shimadzu, Japan) spectrophotometer with a BaSO<sub>4</sub> reference.

### 2.6. Electrochemical measurements

Photocurrent measurements and electrochemical impedance spectroscopy (EIS) tests were carried out on a CHI-760E electrochemical workstation (Chenhua Instrument, Shanghai, China) in a standard three-electrode system. Namely, a saturated calomel electrode (SCE) was used as the reference electrode, a Pt foil as the counter electrode, and the samples as the working electrodes. A 0.5 mol·L<sup>-1</sup> Na<sub>2</sub>SO<sub>4</sub> (pH = ~6) aqueous solution was utilized as the electrolyte. The working electrodes were prepared as follows: 5 mg of the sample was dispersed in 0.5 mL DMF and ultrasonicated for 30 min, then 0.1 mL of colloidal solution was dropped on a 1.5 cm × 1.0 cm indium-tin oxide (ITO) glass substrate with an active area of about 1 cm<sup>2</sup> and allowed to dry at 100 °C overnight. For photocurrent measurements, a 300 W xenon lamp (CEL-HXF300) served as the light source. Mott-Schottky plot was tested at the same conditions with Ag/AgCl reference electrode instead of SCE and without light irradiation.

### 2.7. Photocatalytic oxidation of aromatic alcohol

The photocatalytic oxidation of benzyl alcohol was carried out under a 300 W Xenon lamp (CEL-HXF300, a CEL-VisREF filter, 350–780 nm), 10 cm to the reaction liquid) at ambient temperature (~20 °C). In general, 100 mg of the as-prepared photocatalyst was

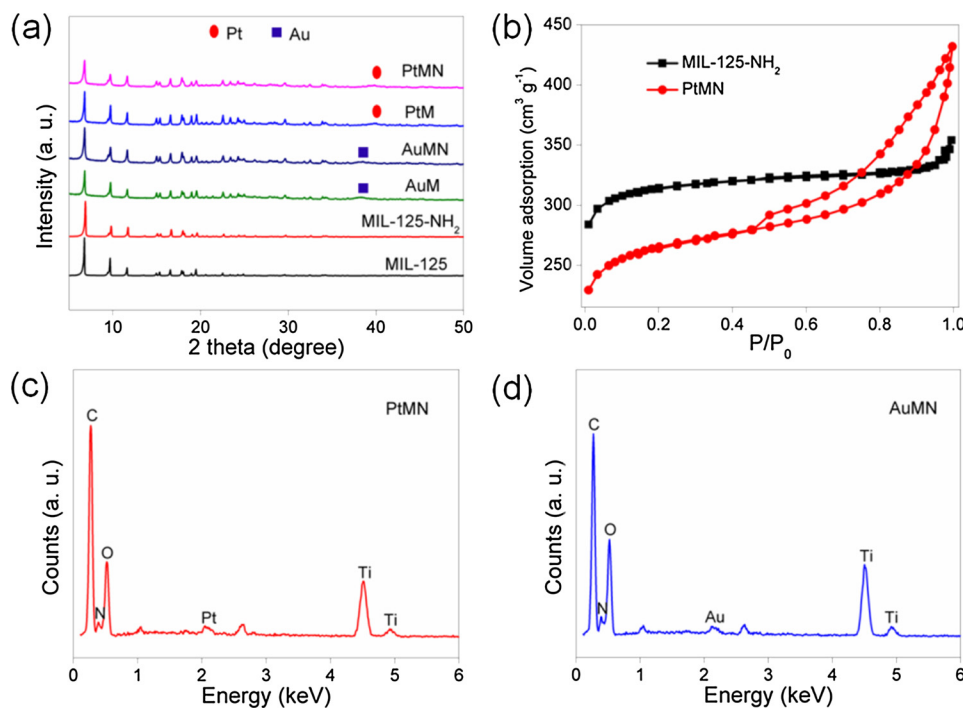


Fig. 1. XRD patterns of all samples (a), N<sub>2</sub> adsorption-desorption isotherms of MIL-125-NH<sub>2</sub> and PtMN (b), EDX images of PtMN (c) and AuMN (d).

dispersed in 20 mL of aromatic alcohol/toluene aqueous solution (0.05 mol·L<sup>-1</sup>) containing 0.035 mol·L<sup>-1</sup> of naphthalene as the internal standard under constant stirring. The choice of solvent toluene was due to its inertness to oxidation and high solubility for molecular O<sub>2</sub>. Prior to illumination, the solution was kept in dark for 60 min under stirring to rule out the influence of adsorption. After illumination for 4 h, an equal volume of liquid sample was obtained by a syringe to filter the catalysts with 0.22 μm filter. Then the analytical sample was analyzed by a GC (Agilent 7820) equipped with an FID and the HP-5 column. To evaluate the stability, the spent catalyst was collected after the photocatalytic reaction by centrifugation, washing with ethanol and drying for the next test.

### 3. Results and discussion

#### 3.1. Materials characterizations

Fig. 1a shows XRD patterns of M/Ti-MOFs and Ti-MOFs. MIL-125-NH<sub>2</sub> and MIL-125 have consistent peaks with previous reports [35,37], indicating the successful synthesis of the two Ti-MOFs. Both Pt and Au loading do not influence the crystallinity of Ti-MOFs, suggesting its good stability. Except the diffraction peaks corresponding to those of Ti-MOFs, the characteristic 2θ peaks at 39.9° in PtMN and PtM (marked by red bulks) ascribed to Pt (111) plane and peaks at 38.3° in AuMN and AuM (marked by blue bulks) assigned to the (111) crystal facet of Au could be observed [27,38], demonstrating the formation of small Pt and Au NPs on Ti-MOFs. It is known that metal NPs loading would decrease the specific surface area of support. Here we chose MIL-125-NH<sub>2</sub> and PtMN as the representatives to reflect the change of surface areas. As shown in Fig. 1b, the isotherm of MIL-125-NH<sub>2</sub> is ascribed to the typical type I according to its microporous structure. A H3 typical hysteresis loop appeared after Pt NPs loading, indicating the presence of slit-like pores and the formation of mesopores and macropores during the NPs loading process [39]. The BET surface area of PtMN (896 m<sup>2</sup> g<sup>-1</sup>) do have a decrease compared to that of MIL-125-NH<sub>2</sub> (1052 m<sup>2</sup> g<sup>-1</sup>) owing to the blockage of pores by Pt NPs. Such high surface areas could provide enough catalytic active sites. Energy-dispersive X-ray spectroscopy (EDX) was utilized to confirm the elemental composition of M/Ti-

MOF. The EDX images of PtMN and AuMN are shown in Fig. 1c and d, which revealed that the M/MIL-125-NH<sub>2</sub> contain C, N, O, Ti and Pt/Au.

Transmission electron microscopy (TEM) images could intuitively reflect the micro morphology and metal loading distribution of Ti-MOFs and M/Ti-MOFs. As shown in Fig. 2a and b, pristine MIL-125-NH<sub>2</sub> exhibited regular and tidy octahedron morphologies with a size about 500–800 nm. The morphologies of MIL-125-NH<sub>2</sub> retained after Pt and Au loading and plenty of NPs homogeneously dispersed on the surface of MIL-125-NH<sub>2</sub> (Fig. 2c and e) with major sizes of 3–9 nm (Fig. 2g and h, drawn by 100 NPs sizes of Pt and Au, respectively), owing to the ultrahigh surface area and porosity of MIL-125-NH<sub>2</sub> and the efficient synthetic method. In addition, the well dispersed metal NPs could facilitate the photo-induced electrons transfer, which is beneficial for the photocatalytic reaction. The HRTEM images in Fig. 2d and f clearly display the lattice fringes of 0.226 and 0.231 nm for Pt and Au NPs respectively. They can be ascribed to the (111) planes of noble metals [25] and these exposed (111) crystal faces of Pt and Au NPs are in complete agreement with their diffraction peaks of XRD.

The TEM images of Pt and Au NPs loading on MIL-125 have also been exhibited in Fig. 3. Unlike to the octahedron morphologies of MIL-125-NH<sub>2</sub>, MIL-125 shows a round pie-like particle with sizes of ca 800–1200 nm (Fig. 3a and b). A mass of Pt and Au NPs adheres uniformly on the surface of MIL-125, indicating the successful synthesis of M/MIL-125 photocatalysts.

XPS analysis is an effective approach to verify the chemical states of each element and interactions between them (Fig. 4). Pt 4f region exhibits peaks at 72.4 and 75.8 eV for Pt<sup>0</sup> 4f<sub>7/2</sub> and Pt<sup>0</sup> 4f<sub>5/2</sub>, demonstrating the successful reduction of Pt<sup>4+</sup> to Pt<sup>0</sup> (Fig. 4a) [25]. Similarly, Au 4f<sub>7/2</sub> and 4f<sub>5/2</sub> peaks at 83.9 and 87.6 eV are attributed to the reduced form of Au<sup>0</sup> (Fig. 4b) [38]. MIL-125-NH<sub>2</sub> shows Ti 2p spectra with binding energy values of 458.4 and 464.2 eV for Ti 2p<sub>3/2</sub> and Ti 2p<sub>1/2</sub>, indicating that titanium remains in oxidation state of Ti(IV) in the titanium-oxo cluster (Fig. 4c). However, the two peaks for PtMN (Ti 2p<sub>3/2</sub>: 458.5 eV, Ti 2p<sub>1/2</sub>: 464.7 eV) and AuMN (Ti 2p<sub>3/2</sub>: 458.7 eV, Ti 2p<sub>1/2</sub>: 464.7 eV) shift a little to higher binding energy, suggesting the existence of chemical interactions between metal nanoparticles and titanium. Interestingly, it is noted that an additional peak appeared in 460 eV for PtMN and 459.7 eV for AuMN, corresponding to the



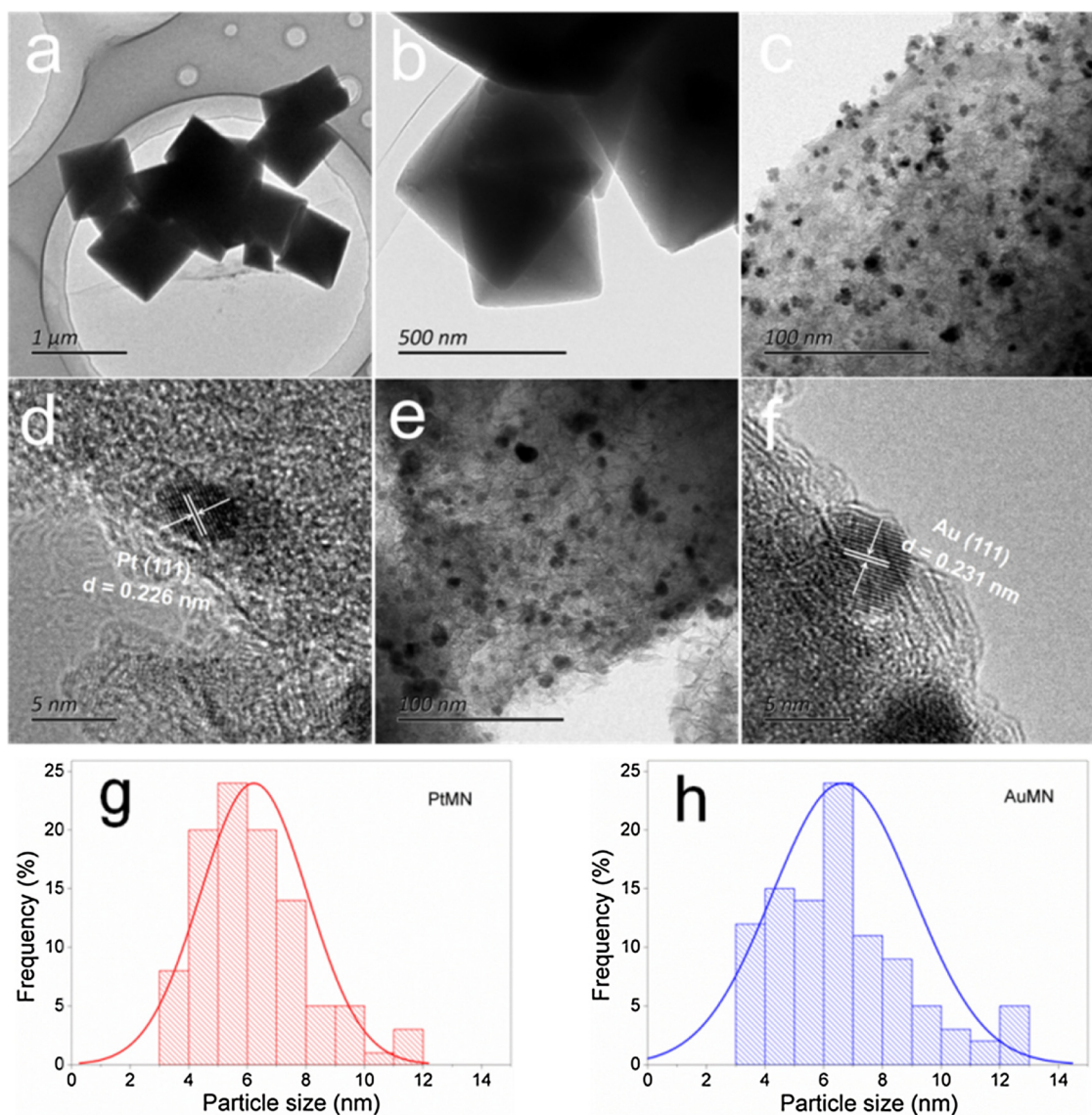


Fig. 2. TEM images of MIL-125-NH<sub>2</sub> (a, b), PtMN (c, d) and AuMN (e, f), Pt and Au particle sizes distributions in PtMN (g) and AuMN (h).

appearance of some Ti<sup>3+</sup> according to the previous report [40]. Ti<sup>3+</sup> ions could decrease the bandgap energy since they have a lower conduction band work function [40], which is helpful for photocatalytic reaction. Two peaks at 399.5 eV and 402.3 eV for MIL-125-NH<sub>2</sub> are ascribed to the N of the amine functionality stretching out or protruding into the cavities (Fig. 4d) [38]. One peak shifts to a lower binding energy from 399.5 eV for MIL-125-NH<sub>2</sub> to 399.2 eV for PtMN and 399.1 eV for AuMN, which further proved the chemical interaction between metal NPs and MIL-125-NH<sub>2</sub>. This chemical interaction would promote metal NPs dispersion and fixation, leading to an efficient reaction activity and recycling.

### 3.2. Photocatalytic performance

The photocatalytic activities of Ti-MOFs and M/Ti-MOFs were evaluated by the photocatalytic selective oxidation of benzyl alcohol and the results are shown in Table 1. The MIL-125-NH<sub>2</sub> occurs a red shift to visible light region compared to MIL-125, leading to a notably enhancement of benzyl alcohol conversion from 5.5% to 13.6% (Entry 5 and 1). Noble metal NPs possess a high work function (5.7, 5.1 and 4.3 eV for Pt, Au and Ag, respectively) [41,42], corresponding to a relative low Fermi level which is promoted for the formation of Schottky

barrier between NPs and scaffold. Besides, some metal NPs such as Au and Ag would produce Localized Surface Plasmon Resonance (LSPR) effect, which enhances the visible-light absorption in a certain degree. The alcohol oxidation conversion of PtMN is 33.1% (Entry 3, 22.7% for 0.5 wt% Pt loading (Entry 2) and 20.9% for 2 wt% Pt loading (Entry 4) indicated that 1 wt% Pt loading (PtMN) is the best mass ratio), which is about 2.4 times and 1.9 times to that of MIL-125-NH<sub>2</sub> (13.6%, Entry 1) and AuMN (17%, Entry 5), respectively. The above results demonstrate that the photocatalytic alcohol oxidation activity of Pt NPs loading is higher than that of Au loading, due to the higher work function of Pt. These results also indicated that the LSPR effect of Au has a negligible improvement to the activity of AuMN. However, the conversions present limited increase after both Pt and Au loading on MIL-125 (Entry 6, 7 and 8), probably because MIL-125 has no visible-light absorption (light absorption edge: 350 nm) and would not generate enough photo-induced electrons. Pt-Au alloy with 0.5 wt%Pt and 0.5 wt%Au loading on MIL-125-NH<sub>2</sub> has an intermediate conversion (21% (Entry 9) compared to that of PtMN and AuMN, suggesting that the alloy loading through this method shows no more improvement to photocatalytic activity. It is noted that all the selectivity is high to 99% which guaranteed the yield of benzaldehyde. No conversion happened when no light or catalyst participated in (Entry 10 and 11), indicating the truth

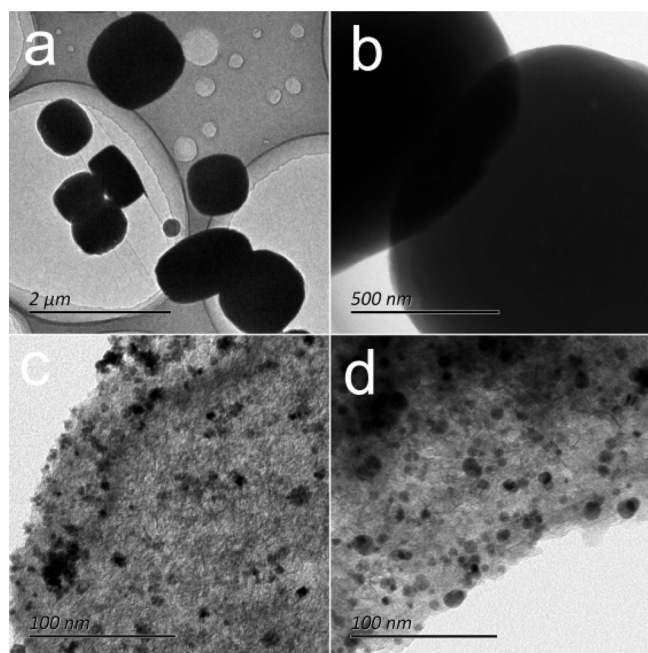


Fig. 3. TEM images of MIL-125 (a and b), PtM (c) and AuM (d).

of photocatalytic activity over M/Ti-MOFs.

To further investigate the photocatalytic oxidation to other aromatic alcohols, methoxybenzyl alcohol and fluorobenzyl alcohol were chosen as the representatives of aromatic alcohols with electron-donating groups and electron-withdrawing groups (Table 2). PtMN was utilized as the photocatalyst. As reported tendencies according to previous reports [43,44], photocatalytic oxidation of methoxybenzyl alcohol had a obvious conversion about 80.3% (Entry 1) while only 19.6% (Entry 2) conversion of fluorobenzyl alcohol was reached. The electron cloud density of the aromatic alcohol aggrandizes and electrons of alcohols are liable to be carried off when the introduction of electron-donating

**Table 1**  
Benzyl alcohol oxidation catalyzed by different samples.

Entry	Catalyst	Conversion (%)	Selectivity (%)
1	MIL-125-NH <sub>2</sub>	13.6	> 99
2 <sup>b</sup>	0.5PtMN	22.7	> 99
3	PtMN	33.1	> 99
4 <sup>c</sup>	2PtMN	20.9	> 99
5	AuMN	17.0	> 99
6	MIL-125	5.5	> 99
7	PtM	6.5	> 99
8	AuM	7.9	> 99
9 <sup>d</sup>	PtAuMN	21.0	> 99
10 <sup>e</sup>	PtMN	–	–
11 <sup>f</sup>	Blank	–	–

[a] Reaction conditions unless otherwise specified: 100 mg of catalyst, 1 mmol of benzyl alcohol and 0.7 mmol naphthalene in 20 mL of toluene at ambient temperature for 4 h light irradiation. [b] 0.5PtMN means 0.5 wt% of Pt NPs loading on MIL-125-NH<sub>2</sub>; [c] 2PtMN means 2 wt% of Pt NPs loading on MIL-125-NH<sub>2</sub>; [d] PtAuMN means 0.5 wt% of Pt and 0.5 wt% of Au co-existed on MIL-125-NH<sub>2</sub>. [e] In dark. [f] No catalyst.

group (CH<sub>3</sub>O-), leading to a higher conversion of alcohols. On the contrary, aromatic alcohol substituted by electron-withdrawing groups (F-) brings about a relative low conversion [43]. The original GC graphs could reflect the conversion of alcohol and production of aldehyde directly (as shown in Fig. 5), the peaks position of benzyl alcohol (reactant), benzaldehyde (resultant) and naphthalene (internal standard) are in around 1.5, 1.2 and 2.3 min, respectively (Fig. 5a–c). In addition, the peaks position of methoxybenzyl alcohol, p-anisaldehyde, fluorobenzyl alcohol and fluoro benzaldehyde are distributed in about 2.8, 2.7, 1.6 and 1.2 min, respectively (Fig. 5d). The conversion and selectivity data were calculated from the relative peaks area proportion between aromatic alcohol (or aromatic aldehyde) and naphthalene.

In order to verify the enhanced photocatalytic activity for other

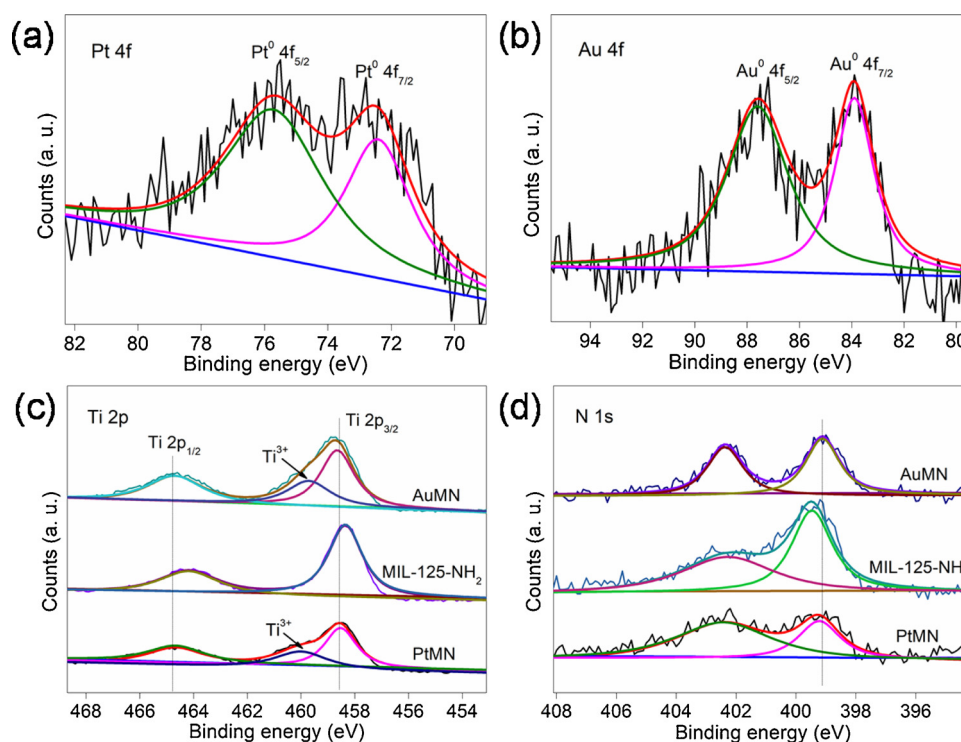
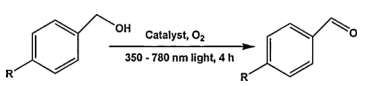
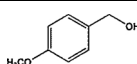
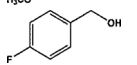


Fig. 4. XPS spectra of PtMN, AuMN and MIL-125-NH<sub>2</sub>: Pt 4f (a), Au 4f (b), Ti 2p (c) and N 1s (d).

**Table 2**  
Aromatic alcohol oxidation catalyzed by PtMN.



Entry	Substrate	Conversion (%)	Selectivity (%)
1		80.3	95
2		19.6	99

Reaction conditions: 100 mg of catalyst, 1 mmol of aromatic alcohol and 0.7 mmol naphthalene in 20 mL of toluene at ambient temperature for 4 h light irradiation.

reaction after Pt loading on MIL-125-NH<sub>2</sub>, Cr(VI) photocatalytic reduction over PtMN and MIL-125-NH<sub>2</sub> has been carried out. As shown in Fig. 6a, MIL-125-NH<sub>2</sub> has a certain photocatalytic activity because of the enhanced visible-light absorption since amino functionalization. A remarkable improvement has been realized after Pt loading, indicating that the existence of Pt NPs accelerated electrons transfer and delayed the recombination of photo-induced electron-hole pairs. Cr(VI) concentration was determined colorimetrically at 540 nm using the diphenylcarbazide method with a detection limit of 0.005 mg L<sup>-1</sup> and the time-dependent absorption spectral patterns of DPC–Cr(VI) complex solutions after reduction over PtMN are shown in Fig. 6b. The reaction sites between active components (<sup>•</sup>O<sub>2</sub><sup>-</sup> or e<sup>-</sup>) and reactants (aromatic alcohol or Cr(VI)) involve at Pt or Au nanoparticles surfaces and MIL-125-NH<sub>2</sub> frameworks.

To know about the specific light absorption of all samples at different wavelengths, UV–vis DRS is an effective approach (Fig. 7). Pristine MIL-125 possesses a light absorption edge of ca 350 nm

(Fig. 7c) and metal (Pt and Au) NPs loading induced a negligible increase of light absorption, which accounts for their non-ideal conversion of alcohol. The introduction of amino functional motif via polyamination of 1,4-benzenedicarboxylate enlarged the light absorption edge to about 510 nm (Fig. 7a). The corresponding decreased band gap energy (2.42 eV) originates from the reduced value band position due to the enhanced electrons density of linker from N 2p spin-orbit, while the conduction band position remains unchanged [45]. The alter of light absorption over metal loading on MIL-125-NH<sub>2</sub> was also limited, which is similar to that of MIL-125. The small change of absorption edge of M/Ti-MOFs mainly because the changes of powder color [46] and the color variations were exhibited in the insets of Fig. 7a and c. To know the band gap energy of M/MIL-125-NH<sub>2</sub> accurately, Kubelka-Munk Equation  $(\alpha hv)^2 = A(hv - E_g)$  has been calculated and the plot of  $(\alpha hv)^2$  versus photo energy (hv) has been fitted into lines (Fig. 7b). MIL-125-NH<sub>2</sub> possesses a band gap energy of 2.42 eV, Pt and Au NPs brought out a little decrease to 2.2 and 2.38 eV respectively, which is probably due to the existence of some Ti<sup>3+</sup> [40]. It is noted that an additional small absorption at 520 nm in AuMN and AuM could be observed, corresponding to the LSPR effect of Au NPs (Fig. 7d). But the enhanced photocatalytic activity triggered by LSPR effect is weak, according to the results of alcohol oxidation (Table 1, entry 3 and 6).

Since UV–vis DRS analyses have demonstrated that the metal loading contributed a little additional light absorption, other proofs to ensure the enhanced photocatalytic activity are needed. Therefore, electrochemical measurements such as photocurrent and Electrochemical Impedance Spectroscopy (EIS) have been conducted (Fig. 8). A rapid photocurrent response over MIL-125-NH<sub>2</sub> and PtMN could be observed for each light-on (10 s) and -off (10 s) (Fig. 8a). Pristine MIL-125-NH<sub>2</sub> has a weak response of photocurrent owing to the fast recombination of photo-induced electrons and holes. It can be seen that an obviously enhanced response of photocurrent was realized by Pt loading, demonstrating that strengthened density and long survival

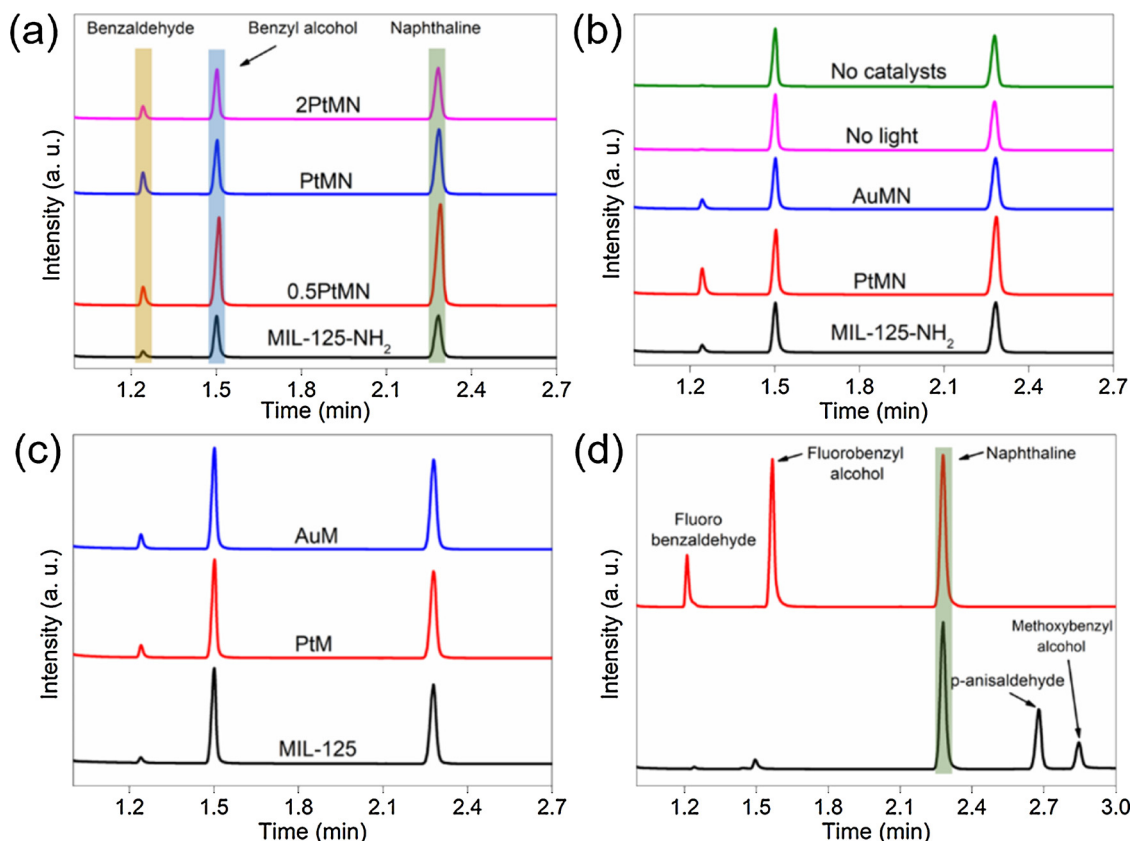


Fig. 5. The spectra of original GC graphs of all samples for benzyl alcohol oxidation (a, b and c) and PtMN for methoxybenzyl and fluorebenzyl alcohol oxidation (d).



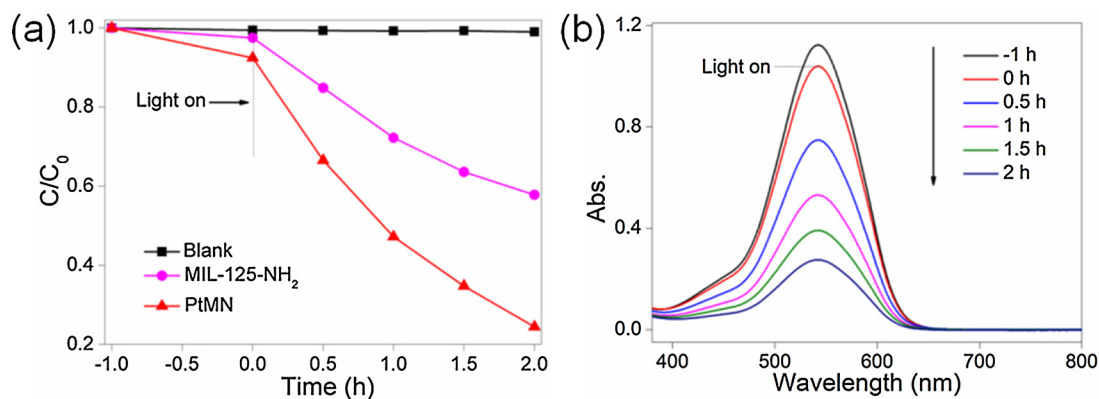


Fig. 6. Photocatalytic reduction of Cr(VI) by MIL-125-NH<sub>2</sub> and PtMN (a). Time-dependent absorption spectral patterns of DPC-Cr(VI) complex solutions after reduction over PtMN (b). Reaction conditions: 40 mg photocatalyst, 40 mL of 15 ppm Cr(VI), pH = 6, ambient temperature.

time of electrons have been produced. The interface charge transports of MIL-125-NH<sub>2</sub> and PtMN have been tested by Electrochemical Impedance Spectroscopy and the EIS Nyquist plots were shown in Fig. 8b (frequency range is 0.1-10<sup>5</sup>). The smaller radius of the arc indicates the faster interfacial transfer on PtMN compared to that of MIL-125-NH<sub>2</sub> [47], which restrained the recombination of photo-induced electrons and holes efficiently. The photocurrent intensity and arc radius of Au/MIL-125-NH<sub>2</sub> locate between Pt/MIL-125-NH<sub>2</sub> and pristine MIL-125-NH<sub>2</sub>, which is well consistent with the performance of photocatalytic benzyl alcohol oxidation. The above two tests of electrochemistry definitely confirmed that the recombination rate of photo-induced electron-hole pairs has been suppressed after Pt loading on MIL-125-NH<sub>2</sub> scaffold, resulting in an outstanding photocatalytic performance for alcohol oxidation and Cr(VI) reduction.

The stability and reusability of photocatalysts are two of important references for practicability. The TEM image of PtMN after reaction has been examined and the image is shown in Fig. 9b. Compared with the image before reaction (Fig. 9a), no apparent agglomeration and

leaching of Pt NPs appeared, demonstrating the good stability of the photocatalysts. In addition, XRD patterns of PtMN before and after photocatalytic reaction exhibit a similar diffraction peaks especially characteristic  $2\theta$  peaks at 39.86° of Pt (Fig. 9c), suggesting that the crystalline and metal loading of used sample remained unchanged. To verify its reusability, photocatalytic oxidation of benzyl alcohol over reclaimed PtMN has been carried out. Neither the conversion nor selectivity have an obvious decrease after four recycle reaction (Fig. 9d), demonstrating the good reusability of M/Ti-MOFs. All the above-mentioned phenomena proved that the high stability of Pt/MIL-125-NH<sub>2</sub> during the photocatalytic reactions.

### 3.3. Proposed mechanism for enhanced photocatalytic activities

Now the specific details of reactions and mechanism for enhanced photocatalytic activity after Pt loading are needed to discuss. To the photo responsive MOFs (e. g. MIL-125 (Ti), UiO-66 (Zr) and MIL-100 (Fe)), organic linkers act as the highest occupied molecular orbital

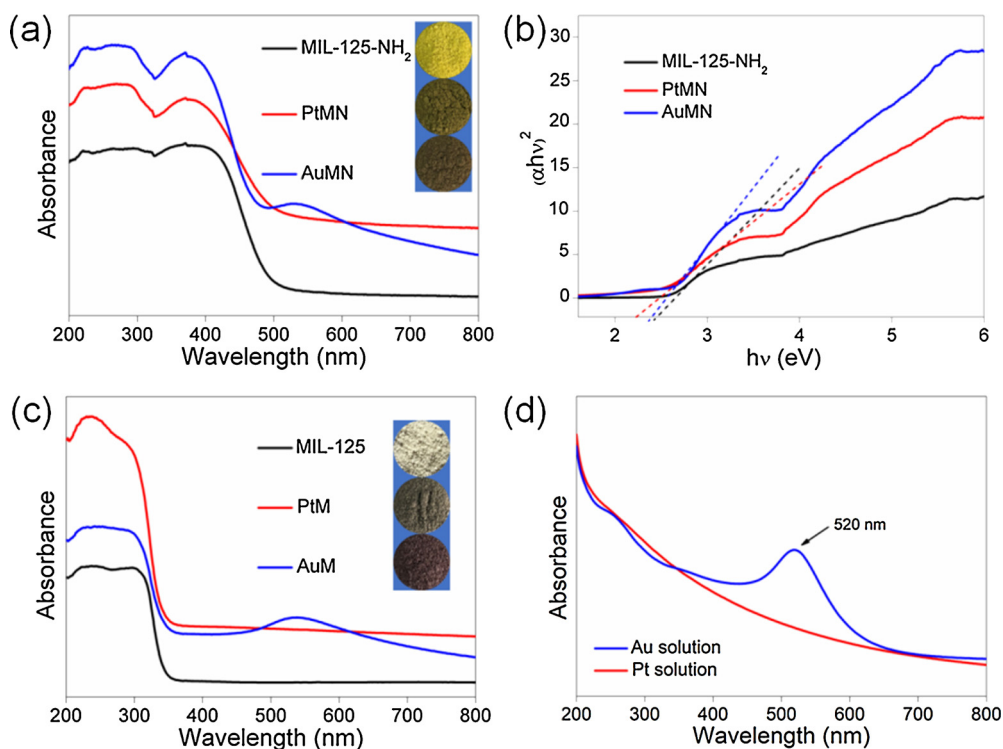
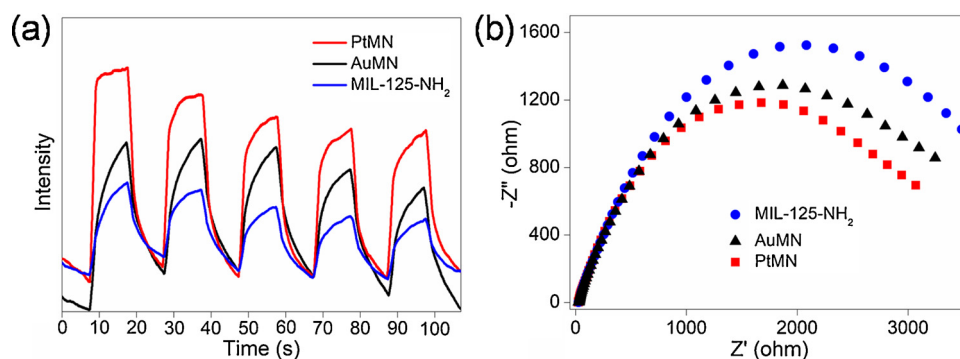


Fig. 7. UV-vis diffuse reflection spectra of MIL-125-NH<sub>2</sub>, PtMN, AuMN (a), MIL-125, PtM, AuM (c), Au and Pt solvent (d),  $(\alpha h\nu)^2$  vs  $h\nu$  curves of MIL-125-NH<sub>2</sub>, PtMN and AuMN (b). The insets of a and c show corresponding colors of these samples.



**Fig. 8.** Photocurrent spectra of PtMN, AuMN and MIL-125-NH<sub>2</sub> under irradiation of 350–780 nm light irradiation with 20 s light on/off cycles (a). EIS Nyquist plots of the three samples under dark condition (b).

(HOMO) and the metallic clusters play the role of lowest unoccupied molecular orbital (LUMO) [48]. Besides, organic linkers always serve as the light antenna especially the amino-functional linkers (proved in Fig. 7a and c). In order to estimate the position of LUMO, Mott-Schottky plot of MIL-125-NH<sub>2</sub> has been done (measurement frequency is 1000) (Fig. 10). The positive plots slope demonstrates that MIL-125-NH<sub>2</sub> was classified to n-type semiconductor materials and its flat band position was about -0.78 eV (intercept value at the x-axis). It is well known that the Fermi level of n-type semiconductor equals to its flat band. Therefore, the LUMO position of MIL-125-NH<sub>2</sub> was estimated to -0.98 eV vs. Ag/AgCl, equivalent to -0.78 eV vs. NHE [49,50].

Since the light irradiation began, electrons (e<sup>-</sup>) existed in HOMO are easily stimulated to the LUMO due to the small band gap energy of MIL-125-NH<sub>2</sub> (2.42 eV, estimated in Fig. 7b) and meanwhile leaving the same amount of holes (h<sup>+</sup>) in the HOMO (Eq. (1)) (Fig. 11). Then electrons will easily transfer to the surface of Pt NPs and Schottky barrier between MIL-125-NH<sub>2</sub> and Pt NPs will be formed. The captured electrons will be released for next reaction. It is well known that superoxide radical (<sup>•</sup>O<sub>2</sub><sup>-</sup>) serves the major active factor for photocatalytic oxidation of aromatic alcohols [37,51,52] (specific <sup>•</sup>O<sub>2</sub><sup>-</sup> radical scavenging experiment in our research has also been done and

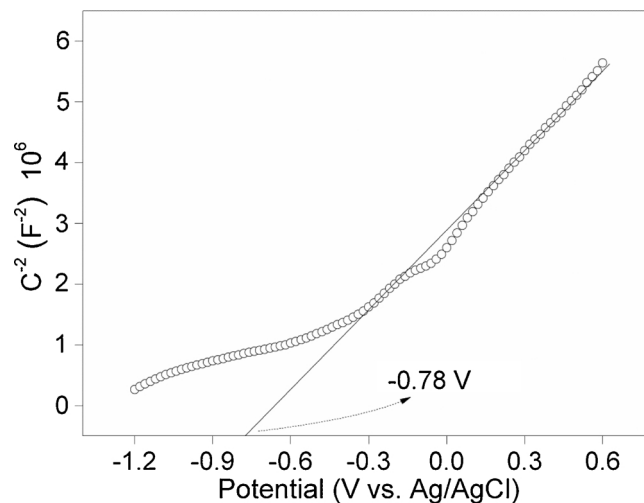


**Fig. 10.** Mott-Schottky plots of MIL-125-NH<sub>2</sub>.

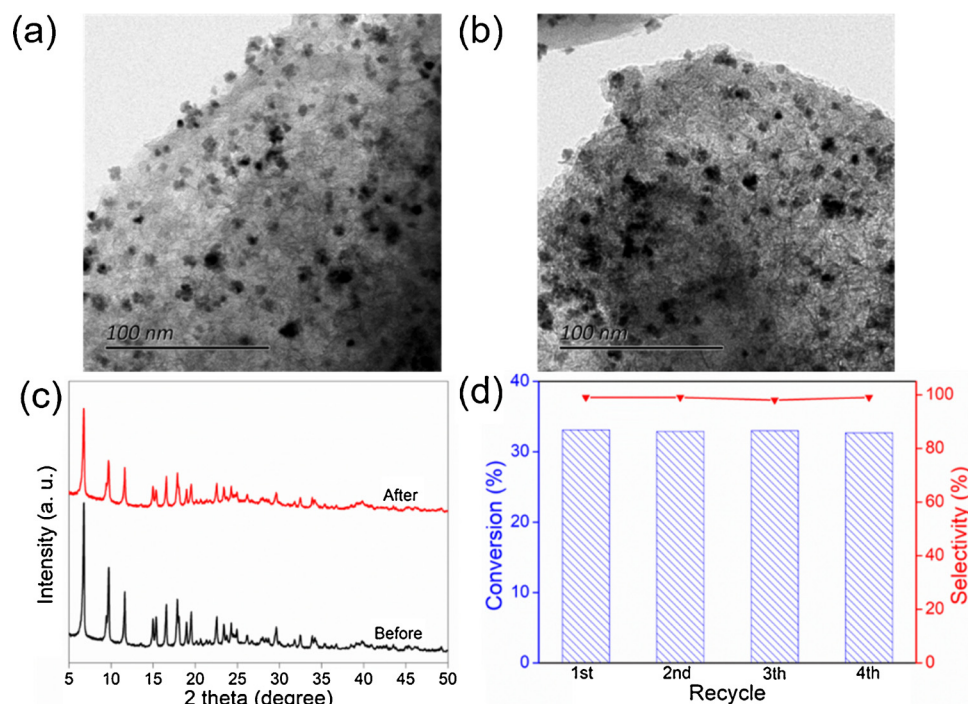


**Fig. 9.** TEM images of PtMN before (a) and after (b) benzyl alcohol photocatalytic oxidation, relative XRD patterns (c) and reusability of PtMN for benzyl alcohol oxidation (d).



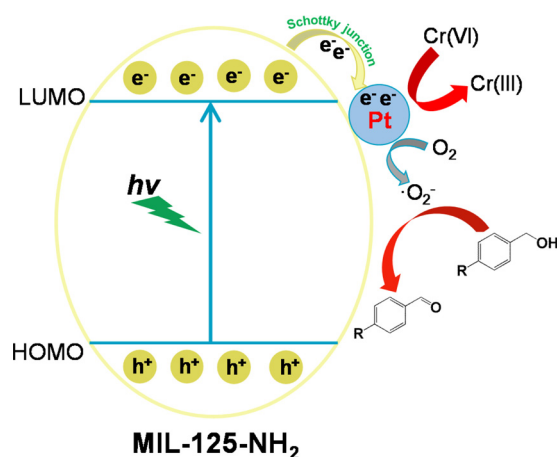
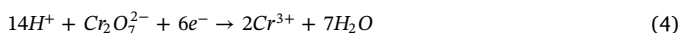
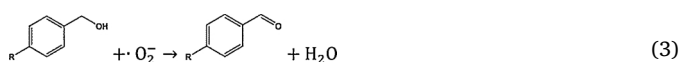


Fig. 11. Proposed mechanism of PtMN for photocatalytic aromatic oxidation and Cr(VI) reduction.

result indicated that the benzyl alcohol conversion decreased from 33.1% to 8.7% after the 1 mM p-benzoquinone ( $\cdot\text{O}_2^-$  scavenger) addition, which is well consistent with the previous reports [37,51,52]) and  $\cdot\text{O}_2^-$  was generated from the  $\text{O}_2$  reduced by  $e^-$  (Eq. (2)). Finally, oxidation reaction between  $\cdot\text{O}_2^-$  and aromatic alcohol occurred and the corresponding aromatic aldehydes have been produced (Eq. (3)). For the photocatalytic reduction of Cr(VI),  $e^-$  could participate in reaction directly (Eq. (4)). The Mott-Schottky plot has proved that the LUMO position of MIL-125-NH<sub>2</sub> is -0.78 eV vs. NHE, which is much negative than that of oxygen reduction ( $\text{O}_2/\cdot\text{O}_2^-$ , -0.28 eV vs. NHE) [53] and Cr (VI) reduction ( $\text{Cr(VI)/Cr(III)}$ , + 0.57 eV vs. NHE) [54], providing the preconditions for two reactions. Meanwhile, water molecules can be oxidized by the holes without the addition of extra scavenger [51,55]. The photocatalytic reaction processes are shown as follows [51,55,56]:



#### 4. Conclusions

In summary, Ti-MOFs (MIL-125 and MIL-125-NH<sub>2</sub>) modifications by highly dispersed Pt or Au NPs have been synthesized by a facile post-synthetic method for the photocatalytic oxidation of benzyl alcohol. TEM analyses verified the good dispersity and the primary size is about 3–9 nm of both Pt and Au. Results showed that the alcohol conversion of metal loading on MIL-125-NH<sub>2</sub> (33.1% for PtMN and 17.0% for AuMN) is much higher than that of MIL-125 (6.5% for PtM and 7.9% for AuM), indicating the importance of light absorption edge on scaffold for metal loading photocatalysis. Pt loading on MIL-125-NH<sub>2</sub> exhibited 2.4 times and 1.9 times as high as that of pristine MIL-125-NH<sub>2</sub> and Au loading respectively for benzyl alcohol photocatalytic oxidation. However, Pt or Au NPs supported on MIL-125 have little increase for the conversion of benzyl alcohol compared to its scaffold. In addition, PtMN also performed well for photocatalytic oxidation of other representative aromatic alcohols and showed much enhanced photocatalytic activity for Cr(VI) reduction. Measurements of photocurrent and Electrochemical Impedance Spectroscopy have verified that the improved photo-induced electron transfer and decreased recombination rates of electron-hole pairs were realized after Pt NPs loading, which

accounts for the enhanced photocatalytic activity of Pt/MIL-125-NH<sub>2</sub>. This work provided considerable information for the noble metal loading on MOFs and amino-functional MOFs in photocatalysis, which is valuable for the design of metal/MOFs or metal/MOFs-NH<sub>2</sub> photocatalysts.

#### Acknowledgments

The authors are grateful for the financial supported by Natural Science Key Project of the Jiangsu Higher Education Institutions (15KJA220001), Priority Academic Program Development of Jiangsu Higher Education Institutions (PAPD). JQ also thanks the financial support from Postgraduate Research & Practice Innovation Program of Jiangsu Province and the Doctorate Fellowship Foundation of Nanjing Forestry University.

#### References

- [1] M. Jia, Y. Feng, S. Liu, J. Qiu, J. Yao, Graphene oxide gas separation membranes intercalated by UiO-66-NH<sub>2</sub> with enhanced hydrogen separation performance, *J. Membr. Sci.* 539 (2017) 172–177.
- [2] J. Qiu, Y. Feng, X. Zhang, M. Jia, J. Yao, Acid-promoted synthesis of UiO-66 for highly selective adsorption of anionic dyes: adsorption performance and mechanisms, *J. Colloid Interf. Sci.* 499 (2017) 151–158.
- [3] J. Yao, H. Wang, Zeolitic imidazolate framework composite membranes and thin films: synthesis and applications, *Chem. Soc. Rev.* 43 (2014) 4470–4493.
- [4] P. Horcajada, T. Chalati, C. Serre, B. Gillet, C. Sebrie, T. Baati, J.F. Eubank, D. Heurtaux, P. Clayette, C. Kreuz, J.-S. Chang, Y.K. Hwang, V. Marsaud, P.-N. Bories, L. Cynober, S. Gil, G. Férey, P. Couvreur, R. Gref, Porous metal-organic-framework nanoscale carriers as a potential platform for drug delivery and imaging, *Nat. Mater.* 9 (2010) 172–178.
- [5] D.Q. Jin, Q. Xu, L.Y. Yu, X.Y. Hu, Photoelectrochemical detection of the herbicide clethodim by using the modified metal-organic framework amino-MIL-125(Ti)/TiO<sub>2</sub>, *Microchim. Acta* 182 (2015) 1885–1892.
- [6] J. Qiu, X. Zhang, K. Xie, X.-F. Zhang, Y. Feng, M. Jia, J. Yao, Noble metal nanoparticle-functionalized Zr-metal organic frameworks with excellent photocatalytic performance, *J. Colloid Interf. Sci.* 538 (2019) 569–577.
- [7] J. Qiu, Y. Feng, X. Zhang, X. Zhang, M. Jia, J. Yao, Facile stir-dried preparation of g-C<sub>3</sub>N<sub>4</sub>/TiO<sub>2</sub> homogeneous composites with enhanced photocatalytic activity, *RSC Adv.* 7 (2017) 10668–10674.
- [8] J. Qiu, X.-F. Zhang, X. Zhang, Y. Feng, Y. Li, L. Yang, H. Lu, J. Yao, Constructing Cd<sub>0.5</sub>Zn<sub>0.5</sub>S@ZIF-8 nanocomposites through self-assembly strategy to enhance Cr (VI) photocatalytic reduction, *J. Hazard. Mater.* 349 (2018) 234–241.
- [9] J. Qiu, X. Zhang, Y. Feng, X. Zhang, H. Wang, J. Yao, Modified metal-organic frameworks as photocatalysts, *Appl. Catal. B-Environ.* 231 (2018) 317–342.
- [10] K. Meyer, R. Ranocchiaro, J.A. van Bokhoven, Metal organic frameworks for photocatalytic water splitting, *Energy Environ. Sci.* 8 (2015) 1923–1937.
- [11] X. Yu, L. Wang, S.M. Cohen, Photocatalytic metal-organic frameworks for organic transformations, *Crystengcomm* 19 (2017) 4126–4136.
- [12] X. Zhang, Y. Yang, W. Huang, Y. Yang, Y. Wang, C. He, N. Liu, M. Wu, L. Tang, g-C<sub>3</sub>N<sub>4</sub>/UiO-66 nanohybrids with enhanced photocatalytic activities for the oxidation of dye under visible light irradiation, *Mater. Res. Bull.* 99 (2018) 349–358.
- [13] R.M. Abdelhameed, D.M. Tobaldi, M. Karmaoui, Engineering highly effective and stable nanocomposite photocatalyst based on NH<sub>2</sub>-MIL-125 encirclement with Ag<sub>3</sub>PO<sub>4</sub> nanoparticles, *J. Photochem. Photobiol. A* 351 (2018) 50–58.
- [14] A. Dhakshinamoorthy, Z. Li, H. Garcia, Catalysis and photocatalysis by metal organic frameworks, *Chem. Soc. Rev.* 47 (2018) 8134–8172.
- [15] Y. Chen, D. Wang, X. Deng, Z. Li, Metal-organic frameworks (MOFs) for photocatalytic CO<sub>2</sub> reduction, *Catal. Sci. Technol.* 7 (2017) 4893–4904.
- [16] C.-C. Wang, J.-R. Li, X.-L. Lv, Y.-Q. Zhang, G. Guo, Photocatalytic organic pollutants degradation in metal-organic frameworks, *Energy Environ. Sci.* 7 (2014) 2831–2867.
- [17] X. Deng, Z. Li, H. Garcia, Visible light induced organic transformations using metal-organic-frameworks (MOFs), *Chem-Eur. J.* 23 (2017) 11189–11209.
- [18] M. Dan-Hardi, C. Serre, T. Frot, L. Rozes, G. Maurin, C. Sanchez, G. Férey, A new photoactive crystalline highly porous titanium (IV) dicarboxylate, *J. Am. Chem. Soc.* 131 (2009) 10857–10859.
- [19] Y. Fu, D. Sun, Y. Chen, R. Huang, Z. Ding, X. Fu, Z. Li, An amine-functionalized titanium metal-organic framework photocatalyst with visible-light-induced activity for CO<sub>2</sub> reduction, *Angew. Chem. Int. Edit.* 51 (2012) 3364–3367.
- [20] D. Sun, L. Ye, Z. Li, Visible-light-assisted aerobic photocatalytic oxidation of amines to imines over NH<sub>2</sub>-MIL-125(Ti), *Appl. Catal. B-Environ.* 164 (2015) 428–432.
- [21] H. Wang, X. Yuan, Y. Wu, X. Chen, L. Leng, G. Zeng, Photodeposition of metal sulfides on titanium metal-organic frameworks for excellent visible-light-driven photocatalytic Cr(VI) reduction, *RSC Adv.* 5 (2015) 32531–32535.
- [22] H. Wang, X. Yuan, Y. Wu, G. Zeng, X. Chen, L. Leng, H. Li, Synthesis and applications of novel graphitic carbon nitride/metal-organic frameworks mesoporous photocatalyst for dyes removal, *Appl. Catal. B-Environ.* 174 (2015) 445–454.
- [23] H. Wang, X. Yuan, Y. Wu, G. Zeng, H. Dong, X. Chen, L. Leng, Z. Wu, In situ synthesis of In<sub>2</sub>S<sub>3</sub>@MIL-125(Ti) core-shell microparticle for the removal of

- tetracycline from wastewater by integrated adsorption and visible-light-driven photocatalysis, *Appl. Catal. B-Environ.* 186 (2016) 19–29.
- [24] H. Goesmann, C. Feldmann, Nanoparticulate functional materials, *Angew. Chem. Int. Edit.* 49 (2010) 1362–1395.
- [25] R. Liang, F. Jing, L. Shen, N. Qin, L. Wu, M@MIL-100(Fe) (M = Au, Pd, Pt) nanocomposites fabricated by a facile photodeposition process: efficient visible-light photocatalysts for redox reactions in water, *Nano Res.* 8 (2015) 3237–3249.
- [26] R. Liang, S. Luo, F. Jing, L. Shen, N. Qin, L. Wu, A simple strategy for fabrication of Pd@MIL-100(Fe) nanocomposite as a visible-light-driven photocatalyst for the treatment of pharmaceuticals and personal care products (PPCPs), *Appl. Catal. B-Environ.* 176 (2015) 240–248.
- [27] L. Chen, Y. Peng, H. Wang, Z. Gua, C. Duana, Synthesis of Au@ZIF-8 single- or multi-core-shell structures for photocatalysis, *Chem. Commun.* 50 (2014) 8651–8654.
- [28] Q. Yang, Q. Xu, S.H. Yu, H.L. Jiang, Pd Nanocubes@ZIF-8: integration of plasmon-driven photothermal conversion with a metal-organic framework for efficient and selective catalysis, *Angew. Chem. Int. Edit.* 55 (2016) 3685–3689.
- [29] D. Wang, Z. Li, Coupling MOF-based photocatalysis with Pd catalysis over Pd@MIL-100 (Fe) for efficient N-alkylation of amines with alcohols under visible light, *J. Catal.* 342 (2016) 151–157.
- [30] D. Sun, M. Xu, Y. Jiang, J. Long, Z. Li, Small-sized bimetallic CuPd nanoclusters encapsulated inside cavity of NH<sub>2</sub>-UiO-66(Zr) with superior performance for light-induced suzuki coupling reaction, *Small Methods* 2 (2018) 1800164.
- [31] D. Wang, Y. Pan, L. Xu, Z. Li, PdAu@MIL-100(Fe) cooperatively catalyze tandem reactions between amines and alcohols for efficient N-alkyl amines syntheses under visible light, *J. Catal.* 361 (2018) 248–254.
- [32] Y. Horiuchi, T. Toyao, M. Saito, K. Mochizuki, M. Iwata, H. Higashimura, M. Anpo, M. Matsuoka, Visible-light-promoted photocatalytic hydrogen production by using an amino-functionalized Ti(IV) metal-organic framework, *J. Phys. Chem. C* 116 (2012) 20848–20853.
- [33] R.M. Abdelhameed, M.M.Q. Simoes, A.M.S. Silva, J. Rocha, Enhanced photocatalytic activity of MIL-125 by post-synthetic modification with Cr-III and Ag nanoparticles, *Chem-Eur. J.* 21 (2015) 11072–11081.
- [34] L. Shen, M. Luo, L. Huang, P. Peng, L. Wu, A clean and general strategy to decorate a titanium metal organic framework with noble-metal nanoparticles for versatile photocatalytic applications, *Inorg. Chem.* 54 (2015) 1191–1193.
- [35] Z. Yang, X. Xu, X. Liang, C. Lei, Y. Cui, W. Wu, Y. Yang, Z. Zhang, Z. Lei, Construction of heterostructured MIL-125/Ag/g-C<sub>3</sub>N<sub>4</sub> nanocomposite as an efficient bifunctional visible light photocatalyst for the organic oxidation and reduction reactions, *Appl. Catal. B-Environ.* 205 (2017) 42–54.
- [36] E. Antolini, Graphene as a new carbon support for low-temperature fuel cell catalysts, *Appl. Catal. B-Environ.* 123 (2012) 52–68.
- [37] Y. Fu, L. Sun, H. Yang, L. Xu, F. Zhang, W. Zhu, Visible-light-induced aerobic photocatalytic oxidation of aromatic alcohols to aldehydes over Ni-doped NH<sub>2</sub>-MIL-125(Ti), *Appl. Catal. B-Environ.* 187 (2016) 212–217.
- [38] D. Sun, W. Liu, Y. Fu, Z. Fang, F. Sun, X. Fu, Y. Zhang, Z. Li, noble metals can have different effects on photocatalysis over metal-organic frameworks (MOFs): a case study on M/NH<sub>2</sub>-MIL-125(Ti) (M = Pt and Au), *Chem-Eur. J.* 20 (2014) 4780–4788.
- [39] J. Yu, S. Wang, J. Low, W. Xiao, Enhanced photocatalytic performance of direct Z-scheme g-C<sub>3</sub>N<sub>4</sub>-TiO<sub>2</sub> photocatalysts for the decomposition of formaldehyde in air, *Phys. Chem. Chem. Phys.* 15 (2013) 16883–16890.
- [40] P. Karthik, E. Balaraman, B. Neppolian, Efficient solar light-driven H<sub>2</sub> production: post-synthetic encapsulation of a Cu<sub>2</sub>O co-catalyst in a metal-organic framework (MOF) for boosting the effective charge carrier separation, *Catal. Sci. Technol.* 8 (2018) 3286–3294.
- [41] B. Yan, L. Zhang, Z. Tang, M. Al-Mamun, H. Zhao, X. Su, Palladium-decorated hierarchical titania constructed from the metal-organic frameworks NH<sub>2</sub>-MIL-125(Ti) as a robust photocatalyst for hydrogen evolution, *Appl. Catal. B-Environ.* 218 (2017) 743–750.
- [42] Y.-Z. Chen, Z.U. Wang, H. Wang, J. Lu, S.-H. Yu, H.-L. Jiang, Singlet oxygen-engaged selective photo-oxidation over Pt Nanocrystals/Porphyrinic MOF: the roles of photothermal effect and Pt electronic state, *J. Am. Chem. Soc.* 139 (2017) 2035–2044.
- [43] J.-L. Wang, C. Wang, W. Lin, Metal-organic frameworks for light harvesting and photocatalysis, *ACS Catal.* 2 (2012) 2630–2640.
- [44] L.J. Shen, S.J. Liang, W.M. Wu, R.W. Liang, L. Wu, CdS-decorated UiO-66(NH<sub>2</sub>) nanocomposites fabricated by a facile photodeposition process: an efficient and stable visible-light-driven photocatalyst for selective oxidation of alcohols, *J. Mater. Chem. A* 1 (2013) 11473–11482.
- [45] H. Wang, X. Yuan, Y. Wu, G. Zeng, X. Chen, L. Leng, Z. Wu, L. Jiang, H. Li, Facile synthesis of amino-functionalized titanium metal-organic frameworks and their superior visible-light photocatalytic activity for Cr(VI) reduction, *J. Hazard. Mater.* 286 (2015) 187–194.
- [46] D. Sun, Z. Li, Double-solvent method to pd nanoclusters encapsulated inside the cavity of NH<sub>2</sub>-UiO-66(Zr) for efficient visible-light-promoted suzuki coupling reaction, *J. Phys. Chem. C* 120 (2016) 19744–19750.
- [47] M. Gao, M.S. Hazelbaker, R. Kong, M.E. Orazem, Mathematical model for the electrochemical impedance response of a continuous glucose monitor, *Electrochim. Acta* 275 (2018) 119–132.
- [48] Y. Li, H. Xu, S. Ouyang, J. Ye, Metal-organic frameworks for photocatalysis, *Phys. Chem. Chem. Phys.* 18 (2016) 7563–7572.
- [49] X. Wang, X. Zhao, D. Zhang, G. Li, H. Li, Microwave irradiation induced UiO-66-NH<sub>2</sub> anchored on graphene with high activity for photocatalytic reduction of CO<sub>2</sub>, *Appl. Catal. B-Environ.* 228 (2018) 47–53.
- [50] G. Zhou, M.-F. Wu, Q.-J. Xing, F. Li, H. Liu, X.-B. Luo, J.-P. Zou, J.-M. Luo, A.-Q. Zhang, Synthesis and characterizations of metal-free Semiconductor/MOFs with good stability and high photocatalytic activity for H<sub>2</sub> evolution: a novel Z-Scheme heterostructured photocatalyst formed by covalent bonds, *Appl. Catal. B-Environ.* 220 (2018) 607–614.
- [51] X. Li, Y. Pi, Q. Hou, H. Yu, Z. Li, Y. Li, J. Xiao, Amorphous TiO<sub>2</sub>@NH<sub>2</sub>-MIL-125(Ti) homologous MOF-encapsulated heterostructures with enhanced photocatalytic activity, *Chem. Commun.* 54 (2018) 1917–1920.
- [52] Z. Wu, X. Huang, H. Zheng, P. Wang, G. Hai, W. Dong, G. Wang, Aromatic heterocycle-grafted NH<sub>2</sub>-MIL-125(Ti) via conjugated linker with enhanced photocatalytic activity for selective oxidation of alcohols under visible light, *Appl. Catal. B-Environ.* 224 (2018) 479–487.
- [53] Y. Cui, J. Huang, X. Fu, X. Wang, Metal-free photocatalytic degradation of 4-chlorophenol in water by mesoporous carbon nitride semiconductors, *Catal. Sci. Technol.* 2 (2012) 1396–1402.
- [54] X.L. Wang, S.O. Pehkonen, A.K. Ray, Removal of aqueous Cr(VI) by a combination of photocatalytic reduction and coprecipitation, *Ind. Eng. Chem. Res.* 43 (2004) 1665–1672.
- [55] R. Djellabi, M.F. Ghorab, Photoreduction of toxic chromium using TiO<sub>2</sub>-immobilized under natural sunlight: effects of some hole scavengers and process parameters, *Desalin. Water Treat.* 55 (2015) 1900–1907.
- [56] H. Wang, X.Z. Yuan, Y. Wu, G.M. Zeng, X.H. Chen, L.J. Leng, Z.B. Wu, L.B. Jiang, H. Li, Facile synthesis of amino-functionalized titanium metal-organic frameworks and their superior visible-light photocatalytic activity for Cr(VI) reduction, *J. Hazard. Mater.* 286 (2015) 187–194.